



Recursive Variational Autoencoders for 3D Blood Vessel Generative Modeling

Paula Feldman^{a,b,*}, Miguel Fainstein^b, Viviana Siless^b, Claudio Delrieux^{a,c}, Emmanuel Iarussi^{a,b}

^aConsejo Nacional de Investigaciones Científicas y Técnicas, Argentina

^bUniversidad Torcuato Di Tella, Buenos Aires, Argentina

^cDepto. Ing. Eléctrica y Computadoras, Universidad Nacional del Sur, Bahía Blanca, Argentina

ARTICLE INFO

Article history:

2000 MSC: 41A05, 41A10, 65D05, 65D17

Keywords: Vascular 3D model, Generative modeling, Neural Networks

ABSTRACT

Anatomical trees play an important role in clinical diagnosis and treatment planning. Yet, accurately representing these structures poses significant challenges owing to their intricate and varied topology and geometry. Most existing methods to synthesize vasculature are rule based, and despite providing some degree of control and variation in the structures produced, they fail to capture the diversity and complexity of actual anatomical data. We developed a Recursive variational Neural Network (RvNN) that fully exploits the hierarchical organization of the vessel and learns a low-dimensional manifold encoding branch connectivity along with geometry features describing the target surface. After training, the RvNN latent space can be sampled to generate new vessel geometries. By leveraging the power of generative neural networks, we generate 3D models of blood vessels that are both accurate and diverse, which is crucial for medical and surgical training, hemodynamic simulations, and many other purposes. These results closely resemble real data, achieving high similarity in vessel radii, length, and tortuosity across various datasets, including those with aneurysms. To the best of our knowledge, this work is the first to utilize this technique for synthesizing blood vessels.

© 2025 Elsevier B. V. All rights reserved.

1. Introduction

Accurate 3D representations are becoming increasingly essential for modeling complex hierarchical structures such as blood vessels, renal tubules, airways, and similar systems. These models play an important role in various domains, ranging from disease diagnosis Roman et al. (2012) and prognosis Murthy et al. (2012) to intervention simulation Le Bras et al. (2023). Another vital application is surgical planning Lawaetz et al. (2021), and fluid dynamics simulation Taylor et al. (2023), among others. The significance of such detailed models extends

beyond the medical domain to fields like computer graphics (i.e. vegetation generation Lee et al. (2023); Cuntz et al. (2010); Banerjee et al. (2020)).

Depending on the downstream task, different data structures may be used to effectively represent the 3D model. Obtaining such representations from patient scans with high resolution and fidelity is not trivial, requires expert medical knowledge, and is highly error-prone Lan et al. (2018); Mou et al. (2024). Despite significant advances in vessel segmentation Tetteh et al. (2020), reconstructing thin features accurately from medical images remains challenging Alblas et al. (2021). As a result, several methods have been developed to adequately synthesize the geometry of blood vessels Wu et al. (2013). Moreover, these generative models are often seen as an opportunity to address the scarcity of data on rarer anatomical and pathological variations van Breugel et al. (2024).

*Corresponding author:

e-mail: paulafeldman@conicet.gov.ar (Paula Feldman)

⁰Code and live demo are available at github.com/LIA-DiTella/vesselvae.

This is the author's accepted manuscript of a paper accepted for publication in Medical Image Analysis (Elsevier). The final version is available at: [].

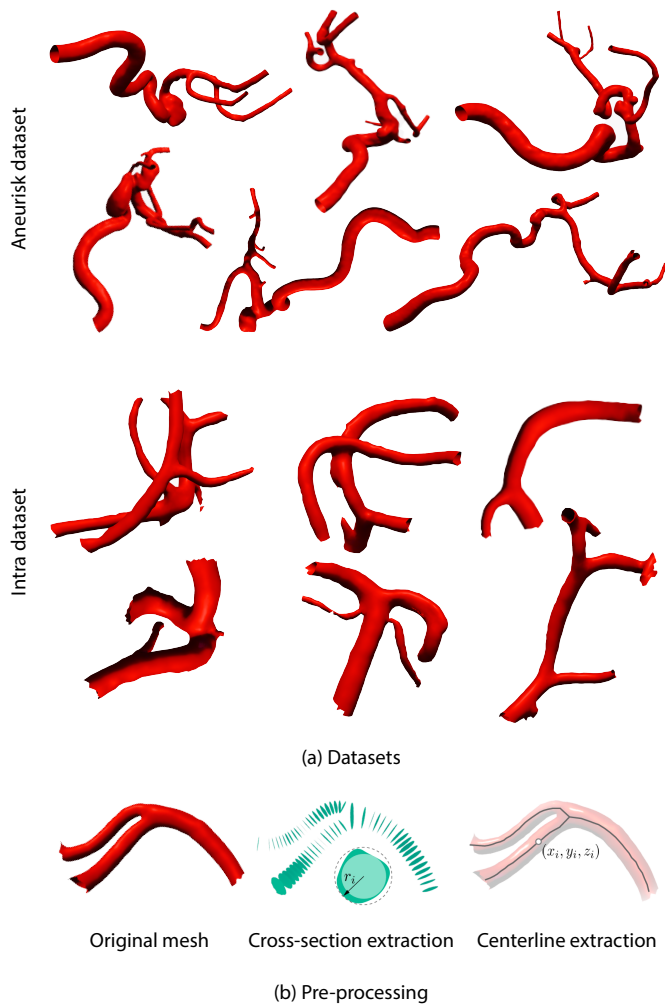


Fig. 1. Datasets and pre-processing overview: The raw meshes from the Intra 3D collection undergo pre-processing using the VMTK toolkit. This step is crucial for extracting centerlines and cross-sections from the meshes, which are then used to construct their binary tree representations.

Within the literature on generating vascular 3D models, we identified two main families: fractal-based, and space-filling algorithms. Fractal-based algorithms use a set of fixed rules that include different branching parameters, such as the ratio of asymmetry in arterial bifurcations and the relationship between the diameter of the vessel and the flow Galarreta-Valverde et al. (2013); Zamir (2001). On the other hand, space-filling algorithms enable blood vessels to grow within a defined perfusion volume while adhering to hemodynamic laws with constraints related to flow and radius Hamarneh and Jassi (2010); Talou et al. (2021); Schneider et al. (2012); Merrem et al. (2017); Rauch and Harders (2021). Although these *model-based* methods provide some degree of control and variation in the structures produced, they often fail to capture the complexity and diversity of real anatomical data. Additionally, the parameter space exploration for desirable results is very haphazard.

In recent years, deep neural networks led to the development of powerful generative models Xu et al. (2023), such as Generative Adversarial Networks (GANs) Goodfellow et al. (2020); Kazemini et al. (2020), Diffusion Models Ho et al. (2020),

and Transformers Vaswani et al. (2017); Siddiqui et al. (2024), demonstrating groundbreaking performance in many applications, ranging from image and video synthesis to protein structure synthesis Ramesh et al. (2021); Yan et al. (2021); Jumper et al. (2021). These advances have inspired the creation of novel network architectures to model 3D shapes using voxel representations Wu et al. (2016), point clouds Yang et al. (2019), signed distance functions Park et al. (2019), and polygonal meshes Nash et al. (2020). However, the use of deep learning to model blood vessel structures has been hindered by the lack of high-quality datasets and the complexity inherent in representing tree-like structured data.

A pioneering approach to generating arterial anatomies with deep generative models was introduced in Wolterink et al. (2018). However, their model remained confined to single-channel vessels, making it unsuitable for generating more complex topologies. More recently, a diffusion model was proposed by Sinha and Hamarneh (2024), operating within the space of Implicit Neural Representations to learn vessel tree distributions. Deo et al. (2024) also builds on latent diffusion models, particularly few-shot learning for generating aneurysms geometries. Kuipers et al. (2024) uses diffusion with a set-transformer architecture to generate vessels as point clouds, but requires a post-processing step to reconstruct the centerlines. Prabhakar et al. (2024) introduced a novel graph-based diffusion model capable of handling cycles, yet it primarily targets capillary networks and is limited to generating the vessels' topology without a corresponding 3D mesh.

In a preceding publication, we presented a framework named VesselVAE Feldman et al. (2023) for synthesizing blood vessel geometry. This generative framework is based on a Recursive variational Neural Network (RvNN), that has been successfully applied in various contexts, including natural language Socher et al. (2011); Socher (2014), shape semantics modeling Li et al. (2017, 2019), and document layout generation Patil et al. (2020). In contrast to previous data-driven methods, our recursive network fully exploits the hierarchical organization of the vessel and learns a low-dimensional manifold encoding branch connectivity along with geometry features describing the target surface. Once trained, the VesselVAE latent space is sampled to generate new vessel geometries. In this article we further expand our results and analysis. Specifically, we trained on different datasets of cerebral arteries, including aneurysms. We performed extensive experiments with our synthetically generated datasets to assess the ability of our method to generate high quality vessel geometry. These experiments build upon and enhance our previous research by providing more comprehensive results, thereby offering a deeper understanding of the capabilities of RvNNs in the generation of anatomically plausible vascular structures.

2. Methods

2.1. Input

The network's inputs is a binary tree representation of the blood vessel 3D geometry. Formally, each tree is defined as a tuple (T, \mathcal{E}) , where T is the set of nodes, and \mathcal{E} is the set of

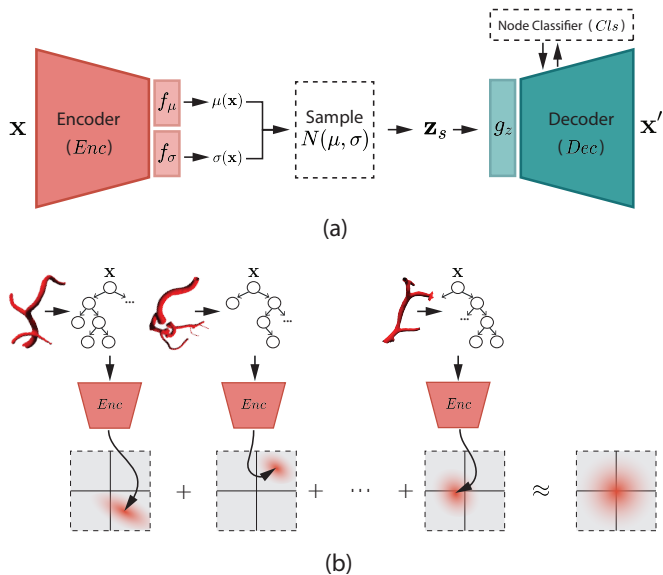


Fig. 2. (a) Overview of the Recursive variational Neural Network for synthesizing blood vessel structures. The architecture follows an Encoder-Decoder framework which can handle the hierarchical tree representation of the vessels. The encoder network (*Enc*) maps a training exemplar to a compact Gaussian distribution in the latent space, while the generator maps a sample from this Gaussian back to the original exemplar. (b) The combination of per-exemplar Gaussians is restricted to match the standard normal distribution (bottom). In the testing phase, drawing samples from the standard normal and decoding them through the generator allows for exploration of the probabilistic manifold captured from the training set. Note that vessel geometry is represented as a binary tree (\mathbf{x}) before being passed through the encoder.

directed edges connecting a pair of nodes (n, m) , with $n, m \in T$. In order to encode a 3D model into this representation, vessel segments are parameterized by a central axis consisting of ordered points in Euclidean space, each point has coordinates x, y, z and radius r , assuming a piece-wise tubular vessel for simplicity. We then construct the binary tree as a set of nodes $T = n_1, n_2, \dots, n_N$, where each node n_i represents a vessel segment and contains an attribute vector $\mathbf{x}_i = [x_i, y_i, z_i, r_i] \in \mathbb{R}^4$ with the coordinates of the corresponding point and its radius r_i . See Sec. 3 for details.

2.2. Network architecture

The proposed generative model is a Recursive variational Neural Network (RvNN) trained to learn a probability distribution over a latent space that can be used to generate new blood vessel segments (Fig. 2). The framework follows an encoder-decoder structure, and the input is a binary tree representation of the vessel \mathbf{x} . During training, the encoder (*Enc*) maps this tree to a compact Gaussian distribution in the learned latent space, ensuring consistency with a standard normal distribution across all training exemplars. After encoding, the decoder (*Dec*) draws samples from a multivariate Gaussian distribution: $\mathbf{z}_s(\mathbf{x}) \sim N(\mu, \sigma)$, with $\mu = f_\mu(\text{Enc}(\mathbf{x}))$ and $\sigma = f_\sigma(\text{Enc}(\mathbf{x}))$, and learns to reconstruct the input vessel anatomies. After training, the RvNN can generate new geometry by drawing samples from

a standard normal distribution and decoding them into novel blood vessel trees \mathbf{x}' .

2.2.1. Encoder network

The encoding process begins with a depth-first post order traversal of the tree \mathbf{x} , recursively encoding each node together with its child nodes, beginning from the leaf nodes until the root node is reached (Fig. 3, (a)). First, the node's attribute vector is processed to produce a partial encoding. If the node has two children, their attribute vectors—along with those of any descendants—are already recursively encoded. The network subsequently processes the latent vectors obtained from the right and left child nodes through additional layers, sums the resulting representations, and then concatenates them with the node's partial encoding. If the node has only one child, the same procedure is followed using a single latent vector. For leaf nodes, a zero vector of the appropriate dimension is concatenated in place of the missing child branches. Ultimately, every node produces a D dimensional encoding that captures the attributes of both the node and its entire sub-tree. Repeating this process up the hierarchy yields a single latent vector representing the entire tree. A more detailed figure illustrating the encoder's internal structure is provided in the supplementary materials. In addition to the core architecture, our Encoder is further augmented with two auxiliary shallow fully-connected neural networks: f_μ and f_σ . Positioned before the RvNN sampling step, these shallow networks shape the distribution of the latent space where the encoded tree structures lie.

2.2.2. Decoder network

The decoding phase reverses the encoding process, reconstructing a binary tree representation \mathbf{x}' from the sampled latent vector \mathbf{z}_s , as depicted in (Fig. 3, (b)). The first step is to decode the root node. Then, on each recursive step, the network decides how many child nodes to decode (one, two, or none). We equipped the decoder with a node classifier module *Cls*, which predicts whether a given latent code corresponds to a leaf node or to an internal node with one or two bifurcations. This is implemented as a multi-layer perceptron trained to predict a three-category bifurcation probability. Complementing the node classifier, the decoder layers are responsible for reconstructing the attribute vectors for each node, specifically its coordinates and radius. Additionally, the decoder can generate up to two extra latent codes (left and right) to enable the recursive decoding of the next node in the hierarchy. If the classifier predicts that only one child is present, we assign it as the right child by default. The Decoder is further augmented with an auxiliary shallow fully-connected neural network: g_z situated after the sampling to facilitate the decoding of latent variables, aiding the Decoder network in the reconstruction of tree structures. Collectively, this supplementary network together with the ones of the Encoder (f_μ and f_σ) streamline the data transformation process through the model. All activation functions used in our networks are leaky ReLUs, except for g_z which uses the Tanh. A complete description of the networks, including a table detailing layers, activation functions, and parameter counts, is provided in the supplementary materials.

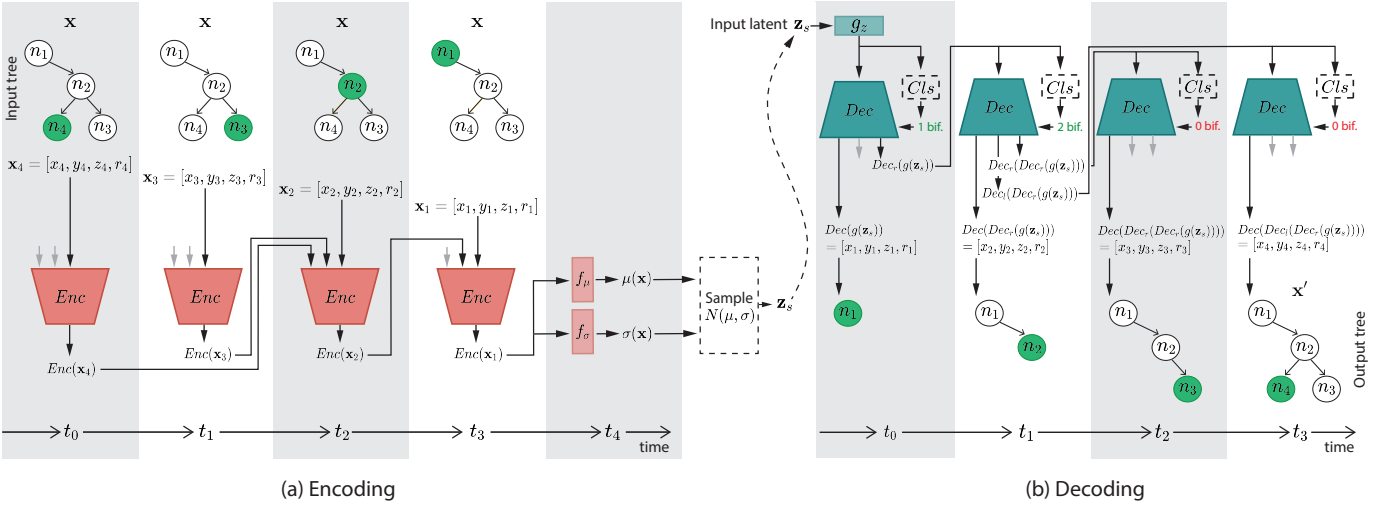


Fig. 3. Proposed encoder-decoder framework. (a) **Encoding.** The input vessel tree is traversed over time steps ($t_0 \rightarrow t_3$, encoding side) from leaves to root. For each node (indicated in green), a feature vector $\mathbf{x}_i = [x_i, y_i, z_i, r_i]$ is processed by the encoder Enc to produce latent embeddings that are ultimately merged into $\mu(\mathbf{x})$ and $\sigma(\mathbf{x})$ parameters of a Gaussian distribution in t_4 . (b) **Decoding.** A sample from this distribution is then fed through the decoder Dec to hierarchically reconstruct the tree ($t_0 \rightarrow t_3$, decoding side). At each step, the model reconstructs output features for the node $\mathbf{x}_i = [x_i, y_i, z_i, r_i]$ and either continues branching or terminates (via the Cls outputs), eventually reproducing the full vessel structure. Green circles highlight nodes created in each step.

2.3. Objective

The encoder-decoder network and the node classifier are trained simultaneously in order to reconstruct the feature vectors \mathbf{x}_i for each node along with the tree topology. For this task, we propose a combined objective function consisting of L_{recon} , which ensures feature vector reconstruction:

$$L_{recon} = \|\text{Dec}(g(\mathbf{z}_s(\mathbf{x}))) - \mathbf{x}\|_2. \quad (1)$$

Note that $\mathbf{z}_s(\mathbf{x})$ denotes a sample drawn from the latent Gaussian distribution whose parameters are computed from the input \mathbf{x} as described before. We also define a loss term to enforce topological correctness using a three-class cross-entropy loss:

$$L_{topo} = - \sum_{c=1}^3 w_c x_c \log(p_c). \quad (2)$$

For each node, $p_c = \text{Cls}(\text{Dec}(g(\mathbf{z}_s(\mathbf{x}))))_c$ denotes the predicted probability that the node belongs to class c . These probabilities are the output of the classifier, which operates on the features produced by the decoder. The classes represent different topological types of nodes: *leaf nodes* (no children), *internal nodes* (one child), and *bifurcation nodes* (two children). The ground truth label x_c is a one-hot encoded vector that equals 1 if the true class of the node is c , and 0 otherwise. To address class imbalance, each class is weighted by w_c , the inverse of its frequency in the dataset.

Additionally, in line with the general framework proposed by β -VAE Higgins et al. (2017), we incorporated a Kullback-Leibler (KL) divergence term encouraging the distribution $p(\mathbf{z}_s(\mathbf{x}))$ over all training samples \mathbf{x} to move closer to the prior of the standard normal distribution $p(\mathbf{z})$. This regularization term is defined as:

$$L_{KL} = D_{KL}(p(\mathbf{z}_s(\mathbf{x})) \| p(\mathbf{z})). \quad (3)$$

Finally, during training we minimize the following equation:

$$L = (1 - \alpha)L_{recon} + \alpha L_{topo} + \gamma L_{KL}. \quad (4)$$

2.4. 3D mesh synthesis

Several algorithms have been proposed to generate a mesh representation of a 3D surface from a tree-structured centerline Wu et al. (2013). We first converted the centerline to a Signed Distance Function (SDF) defined over the 3D space. We discretize the SDF by computing the shortest voxel-to-centerline distance. The SDF at a voxel position $\mathbf{v} \in \mathbb{R}^3$ is defined as:

$$\text{SDF}(\mathbf{v}) = \min_{\mathbf{c} \in C} (\|\mathbf{v} - \mathbf{c}\|^2 - r(\mathbf{c})^2), \quad (5)$$

where C is the set of points along the centerline, \mathbf{c} is a point on the centerline and $r(\mathbf{c})$ is the radius associated with \mathbf{c} . This equation computes the shortest distance from the voxel position \mathbf{v} to the centerline C , adjusted by radius $r(\mathbf{c})$. We then apply the Marching Cubes algorithm Lorensen and Cline (1998), a widely used technique in computer graphics and computational geometry to convert volumetric data into triangle meshes. This process enabled us to preserve fine anatomical details and spatial relationships within the arterial network and obtain a representation suitable for further analysis. Both the SDF generation and marching cubes algorithm were implemented using scripts from the VMTK toolkit ¹

¹<http://www.vmtk.org/documentation/vmtkscripts.html>

3. Experimental Setup

3.1. Materials

We trained our networks on two different datasets. The first is a subset of the open-access Intra dataset² published by Yang et al. in 2020 Yang et al. (2020). This subset consisted of 100 healthy vessel segments reconstructed from 2D MRA images of patients. We also trained our architecture with the open-access Aneurisk dataset³ published by the Aneurisk-Team (2012). This dataset is composed of 100 vessel segments reconstructed from 3D angiographic images containing healthy vessel segments and aneurysms. See Tab. 1 for details.

As a pre-process, we converted 3D meshes into a binary tree representation and used the *network extraction* script from the VMTK toolkit⁴ to extract the centerline coordinates of each vessel model. The centerline points were determined based on the ratio between the sphere step and the local maximum radius, which was computed using the advancement ratio specified by the user. The radius of the blood vessel conduit at each centerline sample was determined using the computed cross-sections assuming a maximal circular shape (see Fig. 1). To improve computational efficiency during recursive tree traversal, we implemented an algorithm that balances each tree by identifying a new root. The new root guarantees the lowest tree height possible without altering the represented vessel topology. We experimented with trimming the trees to different heights and analyzed the network performance for each height. The decision to use lower tree heights reflects a balance between the computational demands of depth-first tree traversal in each training step and the complexity of the training meshes (see Fig. 1s). Note that it is still possible to train with deeper trees at the expense of higher computational costs.

Non-binary trees were transformed into binary trees through an iterative algorithm designed to split multifurcations into binary bifurcations. For each node with more than two children, the algorithm introduces intermediate nodes with the same position and features as the original. This intermediate nodes are then used to sequentially divide the children into pairs, ensuring that no node has more than two children. The process carefully preserves the original spatial arrangement and attributes of the vessel, altering only the tree topology. We excluded vessel models with loops from our experiments.

3.2. Classifier training strategy

To calculate the L_{recon} loss term, we bypassed the classifier’s predictions and used the original tree topology for decoding during training. This approach allows us to compare node attributes effectively, even if the classifier fails to make accurate topology predictions while being trained to predict the degree of each node. Given the imbalance in node distribution across classes, we adjust the weights in the cross-entropy loss calculation by using the inverse of each class count. During

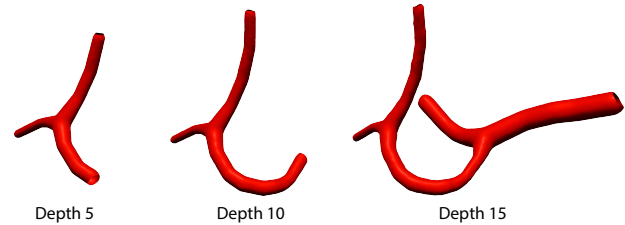


Fig. 4. Representation of tree structures at varying heights: The same vascular tree trimmed to different heights (5, 10, and 15), demonstrating the structural changes and complexity reduction at lower heights.

Height	ϵ	Nodes			Bifurcations
		Min	Max	Avg	Avg
Aneurisk (Aneurisk-Team (2012))					
5	0.2	5	18	10.01	1.86
	0.1	5	18	9.65	1.53
10	0.2	12	43	25.00	3.38
	0.1	10	46	23.02	2.62
15	0.2	22	73	41.56	4.80
	0.1	15	73	38.44	3.73
Intra (Yang et al. (2020))					
5	0.2	6	15	9.67	1.52
	0.1	7	15	9.78	1.46
10	0.2	6	30	14.53	1.69
	0.1	7	35	18.86	1.66
15	0.2	6	34	14.88	1.70
	0.1	7	46	20.64	1.72

Table 1. Node and bifurcation statistics for the Aneurisk and Intra datasets, computed at different tree heights and resampling rates (ϵ).

preliminary experiments, we observed that accurately classifying nodes closer to the tree root is critical. A misclassification at the top levels (closer to the root) can lead to a cascading effect, impacting the reconstruction of all subsequent branches in the tree (i.e. skip reconstructing a branch). To account for this, we implemented and evaluated different weighting schemes assigning a weight to the cross-entropy loss based on the node depth and number of total sub-tree nodes.

3.3. Implementation details

We developed the data preprocessing pipeline and network code using Python, VMTK and the PyTorch Framework. For centerline extraction, we set the VMTK script’s advancement ratio to 1.05. This produces multiple cross-sections at bifurcations, where we select the one with the smallest radius to ensure alignment with the principal centerline direction. All tree attributes were normalized to the range [0, 1]. In our training setup, the batch size was set to 4, and we used the ADAM optimizer with settings $\beta_1 = 0.9$, $\beta_2 = 0.999$, and a learning rate of 1×10^{-4} . For Eq. 4, we used $\alpha = 0.3$ and $\gamma = 0.001$. All models were trained for 20,000 epochs.

To accelerate computation, we implemented dynamic batching Looks et al. (2017), which groups operations for input trees of varying shapes and different nodes within a single graph.

²<https://github.com/intra3d2019/Intra>

³<https://github.com/perfml/AneuriskData>

⁴<http://www.vmtk.org/vmtkscripts/vmtknetworkextraction>

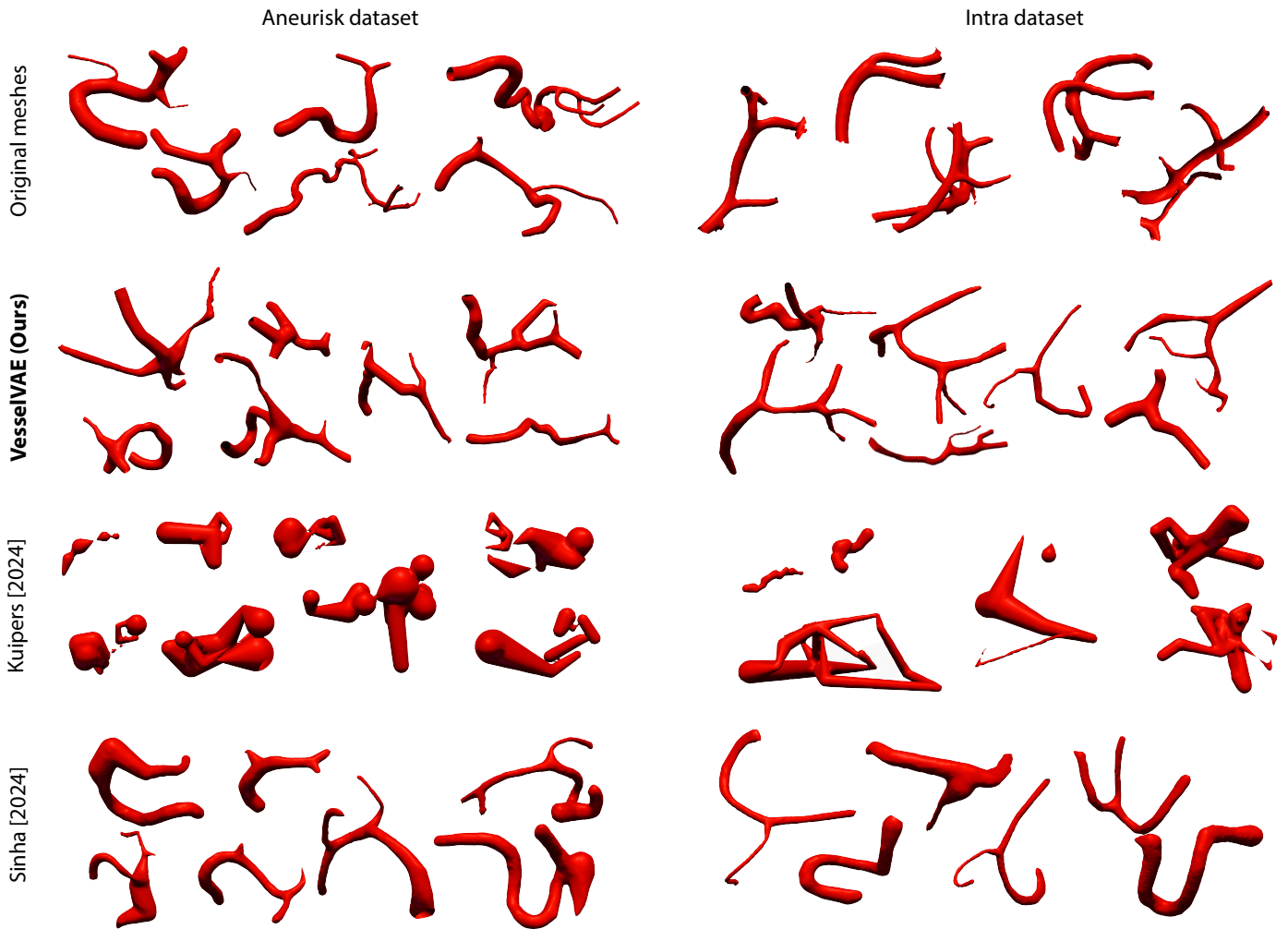


Fig. 5. Comparison of vessel geometries generated by VesselVAE (Ours) and baseline methods trained on the Aneurisk and Intra datasets. The approach by Kuipers *et al.* (2024) struggles with intricate geometry, often producing disconnected segments and failing to capture the underlying feature distribution. Meanwhile, Sinha and Hamarneh (2024) generates proper vessel geometries but lacks diversity, resulting in simpler and shallower structures. In contrast, our method demonstrates superior performance, producing diverse and realistic vessel meshes.

Training time is predominantly influenced by the height of the tree, as deeper trees require more sequential processing steps. Due to the implementation of dynamic batching, all nodes at the same depth are processed simultaneously, reducing the number of sequential steps required to transverse the tree. Consequently, while the amount of ramifications has some impact, it is relatively minor compared to the effect of tree height on training time. This is particularly noticeable with the Aneurisk dataset due to its larger number of ramifications compared to the Intra dataset, see Tab. 1 for more details about the amount of bifurcations and nodes for each dataset. On average, training our models takes between 12 and 36 hours. All experiments were run on a workstation equipped with an NVIDIA A100 GPU, 80GB VRAM, and 256GB RAM.

3.4. Experiments

We trained our generative autoencoders using two different datasets, two different resampling rates, and three maximum heights to investigate how these factors and different hyperparameter choices influence the model’s behavior and generative

capabilities. After preprocessing and discarding vessels with loops, each dataset consisted of 100 samples. We applied resampling to the original trees to better capture their structure with a reduced number of nodes. This was achieved using the Ramer-Douglas-Peucker algorithm Ramer (1972); Douglas and Peucker (1973). Although resampling can affect the height of the original tree, we imposed a fixed maximum during training (5, 10, or 15) to ensure consistency across experiments. The resampling rate, defined by parameters $\epsilon = 0.1$ and $\epsilon = 0.2$, controls the maximum allowable distance between the original and the simplified curve, influencing how well the tree’s geometry is captured within the specified node limit. Additionally, we conducted an ablation study to assess the impact of the weighting scheme on the node classifier behavior.

4. Results

We now evaluate our method against recent approaches (Sec. 4.1), beginning with a comparison with the methods of Sinha and Hamarneh (2024) and Kuipers *et al.* (2024) in

	MMD ↓	COV ↑	1-NNA
Aneurisk			
Sinha and Hamarneh (2024)	1.264	.19	.03
Kuipers et al. (2024)	.537	.03	.0
VesselVAE (Ours)	.004	.58	.68
Intra			
Sinha and Hamarneh (2024)	.447	.22	.1
Kuipers et al. (2024)	.288	.04	.0
VesselVAE (Ours)	.039	.47	.4

Table 2. Quantitative results for novel tree generation comparing our method against baseline approaches. Metrics are denoted as follows: ↑ indicates that higher values are better, ↓ indicates that lower values are better, and for 1-NNA, the optimal score is 0.5. For Sinha and Hamarneh (2024) and Kuipers et al. (2024), we observed low 1-NNA alongside low COV, indicating model collapse: the model produces highly similar samples that cluster in a narrow region of the distribution, sufficiently realistic to fool the 1-NN classifier, but lacking diversity.

Sect. 4.1.1. This is followed by an analysis of results relative to the older baselines proposed by Hamarneh and Jassi (2010) and Wolterink et al. (2018) in Sec. 4.1.2. In Sec. 4.2, we further explore the synthesis of pathological geometry features within vascular structures. Lastly, Sec. 4.3 presents an ablation study to evaluate the impact of relevant training configuration choices.

4.1. Comparison against baseline methods.

4.1.1. Sinha and Hamarneh (2024) and Kuipers et al. (2024)

We quantitatively evaluated the generated samples and compared them to recent methods using three established metrics: Minimum Matching Distance (MMD), Coverage (COV), and 1-Nearest Neighbor Accuracy (1-NNA).

MMD Achlioptas et al. (2018) measures the quality of the generated samples by computing, for each real sample, the distance to its closest counterpart in the generated set and averaging these values. Low MMD values indicate that the generated samples are close to the real ones, suggesting high fidelity and good coverage of the data distribution. COV Achlioptas et al. (2018) quantifies the diversity of the generated distribution by determining the proportion of real samples that can be paired with at least one generated sample. This is done by identifying the closest match in the reference set for each generated sample using a distance function such as Chamfer Distance (CD) or Earth Mover’s Distance (EMD). Higher COV values are desirable, as they indicate that a larger portion of the real distribution is represented by the generated set. Although coverage is effective in detecting mode collapse (e.g. when many generated samples map to the same or a few real samples), it does not provide information about sample quality. In some cases, perfect coverage can be achieved even if the matched pairs are significantly different. Finally, 1-NNA Yang et al. (2019) evaluates the plausibility of the generated distribution by computing the leave-one-out 1-nearest neighbor classification accuracy between real and generated samples. A value close to 50% indicates that the two distributions are well-mixed, while scores significantly above or below this threshold suggest mode collapse or poor generalization.

Our evaluation was performed on both datasets, resampled at a rate of 0.2 and with a depth of 10, as this configuration yielded the best performance in our ablation study. The results are presented in Tab. 2. Our model consistently outperforms both baselines across all three metrics when trained on the same datasets. Additionally, Fig.5 complements the quantitative analysis with example renders for all methods and training datasets. In terms of efficiency, our method is significantly more lightweight, using ~1 million parameters compared to the ~43 million and ~41 million parameters required by Sinha and Hamarneh (2024) and Kuipers et al. (2024), respectively. Furthermore, our model has a much smaller memory footprint during training, requiring ~67MB compared to ~173MB and ~2,000MB for the other methods.

4.1.2. Hamarneh and Jassi (2010)

Comparing synthetic samples with real datasets (such as Aneurisk or Intra) is possible by measuring differences in parameter distributions. However, it is not trivial to compare our approach with other methods such as Vascusynth. This is because procedural and data-driven methods have fundamentally different approaches, making direct comparison challenging.

To make this feasible, we generated a synthetic dataset using the method described in Hamarneh and Jassi (2010) and trained VesselVAE on these data. The goal is to assess whether VesselVAE can generate similar samples while maintaining the expressiveness and precision of the original generative method. In our experiments, the training dataset was resampled with $\epsilon = 0.1$ and $\epsilon = 0.2$ (as with previous comparisons). After training, we computed radius, tortuosity, and length metrics to compare distributions. Table summarizing results can be found in Supplementary Material. Fig. 6 illustrates vessel geometries generated by VesselVAE when trained on Vascusynth data, demonstrating its ability to capture the main geometric characteristics of Vascusynth.

4.2. Pathology geometry synthesis

A key strength of our data-driven approach is its ability to naturally capture and reproduce distinctive geometric features present in the training data. In Fig. 7 we show some synthesized vessel geometries featuring aneurysms after training on the Aneurisk dataset. Unlike parametric methods which require explicit coding to replicate such features, our approach inherently learns and reproduces both realistic non-pathological and pathological vessel structures.

4.3. Ablation

We conducted an ablation study to evaluate the impact of various configurations on our model’s performance. Specifically, we tested three different loss weighting schemes: (1) assigning a *uniform* weight of one to all nodes in the tree, (2) weighting each node based on its *depth* within the tree, and (3) weighting each node according to the size of its *sub-tree*, where each node is treated as the root of its respective sub-tree. Additionally, we explored the effects of two different vessel centerline resampling rates $\epsilon = 0.1$ and $\epsilon = 0.2$ and retrained our models using three different maximum heights (5, 10, and 15). This

Weighting Scheme	Max. Height	ϵ	Cosine Similarity \uparrow						Earth Mover Distance \downarrow					
			Radius		Tortuosity		Length		Radius		Tortuosity		Length	
			M	CI	M	CI	M	CI	M	CI	M	CI	M	CI
Aneurisk(Aneurisk-Team (2012))														
Uniform	5	0.2	.93	(.91 .95)	.88	(.86 .89)	.95	(.93 .97)	.55	(.47 .54)	2.53	(1.99 3.06)	.65	(.48 .82)
Depth			.95	(.93 .96)	.92	(.90 .94)	.96	(.95 .97)	.39	(.28 .49)	1.87	(1.44 2.29)	.45	(.28 .61)
Sub-tree			.94	(.92 .96)	.93	(.91 .94)	.96	(.93 .98)	.43	(.33 .52)	2.24	(1.81 2.66)	.28	(.24 .32)
Uniform		0.1	.94	(.93 .96)	.77	(.72 .83)	.93	(.91 .95)	.49	(.35 .62)	3.1	(2.42 3.79)	.64	(.47 .8)
Depth			.92	(.90 .94)	.83	(.79 .86)	.96	(.94 .97)	.54	(.4 .68)	2.49	(2.13 2.86)	.43	(.33 .53)
Sub-tree			.92	(.91 .94)	.9	(.87 .92)	.95	(.95 .96)	.54	(.41 .66)	2.61	(1.89 3.34)	.39	(.28 .5)
Uniform	10	0.2	.95	(.93 .96)	.86	(.83 .89)	.92	(.9 .94)	.68	(.54 .82)	2.37	(1.99 2.75)	.82	(.67 .97)
Depth			.93	(.90 .95)	.93	(.91 .96)	.96	(.94 .97)	.58	(.44 .72)	1.21	(1.08 1.34)	.38	(.22 .54)
Sub-tree			.96	(.94 .98)	.94	(.92 .95)	.96	(.95 .97)	.58	(.47 .69)	1.15	(.85 1.45)	.36	(.28 .44)
Uniform		0.1	.91	(.9 .93)	.77	(.7 .83)	.86	(.82 .9)	.74	(.55 .94)	3.08	(2.59 3.56)	1.27	(1.12 1.42)
Depth			.94	(.93 .95)	.91	(.88 .95)	.96	(.95 .97)	.49	(.42 .56)	1.5	(1.22 1.79)	.59	(.46 .71)
Sub-tree			.96	(.95 .97)	.93	(.9 .95)	.95	(.93 .97)	.47	(.36 .58)	1.6	(1.15 2.05)	.46	(.29 .63)
Uniform	15	0.2	.83	(.8 .86)	.83	(.81 .85)	.91	(.88 .93)	1.25	(1.14 1.31)	1.92	(1.37 2.48)	1.4	(1.18 1.62)
Depth			.92	(.9 .94)	.83	(.78 .87)	.46	(.4 .51)	.6	(.47 .72)	2.64	(1.87 3.4)	2.72	(2.54 2.91)
Sub-tree			.92	(.9 .95)	.95	(.94 .96)	.94	(.94 .95)	.54	(.42 .65)	1.19	(.96 1.41)	.81	(.71 .91)
Uniform		0.1	.94	(.92 .96)	.74	(.68 .8)	.86	(.84 .88)	.76	(.64 .88)	3.52	(2.82 4.22)	1.6	(1.44 1.76)
Depth			.93	(.92 .95)	.84	(.8 .88)	.72	(.69 .76)	.63	(.52 .73)	2.13	(1.55 2.71)	1.91	(1.8 2.02)
Sub-tree			.94	(.92 .95)	.83	(.81 .86)	.91	(.88 .94)	.77	(.65 .88)	1.79	(1.32 2.26)	.75	(.64 .85)
Intra(Yang et al. (2020))														
Uniform	5	0.2	.97	(.96 .98)	.93	(.92 .94)	.93	(.9 .95)	.55	(.42 .67)	2.38	(1.79 2.97)	.48	(.4 .55)
Depth			.95	(.94 .96)	.93	(.91 .95)	.93	(.91 .95)	.56	(.46 .65)	1.7	(1.3 2.09)	.39	(.32 .46)
Sub-tree			.94	(.92 .96)	.94	(.91 .96)	.94	(.92 .96)	.42	(.29 .56)	1.86	(1.41 2.32)	.52	(.42 .63)
Uniform		0.1	.97	(.96 .98)	.91	(.89 .95)	.95	(.93 .96)	.44	(.35 .53)	2.7	(2.08 3.32)	.42	(.35 .5)
Depth			.9	(.88 .91)	.9	(.87 .94)	.96	(.95 .97)	.59	(.53 .65)	2.64	(1.96 3.31)	.52	(.4 .64)
Sub-tree			.97	(.96 .98)	.9	(.87 .93)	.95	(.93 .97)	.51	(.42 .6)	3.49	(2.3 4.69)	.39	(.33 .45)
Uniform	10	0.2	.95	(.94 .97)	.89	(.87 .92)	.93	(.9 .96)	.66	(.52 .79)	2.33	(1.66 3.0)	.41	(.33 .49)
Depth			.97	(.95 .99)	.97	(.95 .98)	.95	(.94 .97)	.41	(.37 .45)	1.52	(1.06 1.98)	.42	(.32 .53)
Sub-tree			.95	(.93 .97)	.93	(.9 .95)	.96	(.93 .98)	.52	(.42 .61)	1.6	(1.32 1.88)	.31	(.23 .39)
Uniform		0.1	.96	(.94 .97)	.81	(.77 .85)	.95	(.94 .97)	.39	(.34 .43)	2.81	(1.85 3.78)	.68	(.61 .76)
Depth			.94	(.93 .96)	.95	(.93 .97)	.94	(.92 .96)	.56	(.4 .73)	1.39	(1.0 1.78)	.68	(.55 .8)
Sub-tree			.94	(.92 .96)	.86	(.81 .9)	.95	(.92 .97)	.54	(.43 .66)	2.04	(1.74 2.34)	.41	(.25 .56)
Uniform	15	0.2	.94	(.92 .96)	.9	(.88 .93)	.92	(.89 .94)	.67	(.51 .83)	2.11	(1.59 2.62)	.54	(.39 .69)
Depth			.95	(.93 .97)	.96	(.94 .97)	.92	(.9 .94)	.43	(.36 .49)	1.08	(.84 1.31)	.48	(.37 .59)
Sub-tree			.96	(.95 .97)	.94	(.91 .96)	.96	(.95 .98)	.38	(.29 .47)	1.63	(1.33 1.93)	.38	(.29 .47)
Uniform		0.1	.95	(.94 .97)	.88	(.83 .93)	.95	(.93 .97)	.65	(.53 .78)	2.71	(1.85 3.57)	.93	(.75 1.11)
Depth			.96	(.93 .98)	.93	(.9 .96)	.95	(.94 .97)	.54	(.44 .65)	2.6	(2.14 3.06)	1.01	(.82 1.19)
Sub-tree			.94	(.92 .96)	.86	(.81 .91)	.95	(.93 .96)	.67	(.56 .79)	1.64	(1.14 2.14)	.56	(.42 .69)

Table 3. Ablation summary. Cosine Similarity and Earth Mover Distance for all the evaluated metrics with resampling parameter ϵ set to 0.1 and 0.2. All experiments were carried out 10 times with randomized seeds. We report the mean values (M) and 95 % confidence intervals (CI). The weighting scheme column corresponds to loss weight ablation. *Uniform* refers to constant weighting, *Depth* indicates depth-based weighting, and *Sub-tree* corresponds to sub-tree size weighting. In bold the best-performing scheme for trees of depth 10 and resampling rate 0.2. These highlighted models were used for the evaluation in Tab. 2 and Fig. 5

comprehensive evaluation allowed us to analyze the contributions of each factor to the overall performance of the model and select the best-performing configuration for the aforementioned comparisons.

To assess the best-performing model we established a set of metrics: tortuosity per branch, total vessel centerline length, and average tree radius. These metrics have been widely used in the field of 3D modeling of blood vessels, and have been shown to provide reliable and accurate quantification of blood vessels’ main characteristics Bullitt et al. (2003a); Lang et al. (2012); Sinha and Hamarneh (2024). The tortuosity distance metric Bullitt et al. (2003b), a measure of branch twistiness computed as the ratio between each branch’s length and the straight-line distance between its endpoints, has clinical importance in blood vessel analysis. We also evaluated total vessel length and average radius metrics previously used to differentiate healthy from cancerous malformations Bullitt et al. (2003a);

Lang et al. (2012). Due to the inherent randomness in the generation process, we synthesized 10 distinct sets of 100 samples each for every combination of weights, dataset, depth, and resampling rate. Metrics were computed for each training and generated set, and we compared distributions using Cosine Similarity (CS) and Earth Mover’s Distance (EMD). We report the mean values along with 95 % confidence intervals in Tab. 3.

We observed high similarity scores between histograms at depths 5 and 10, indicating that the generated blood vessels are realistic. The slight decrease in similarity at depth 15, particularly for the Aneurisk dataset, is attributed to increased computational demands (see Section 5). The uniform scheme significantly deteriorates the similarity values across all evaluated metrics. The effect of non uniform weighting gains importance when the height of the tree increases, while for shallow trees (height 5 in our experiments) performance remains mostly unaffected. Fig. 8 shows the distribution for the evaluated metrics

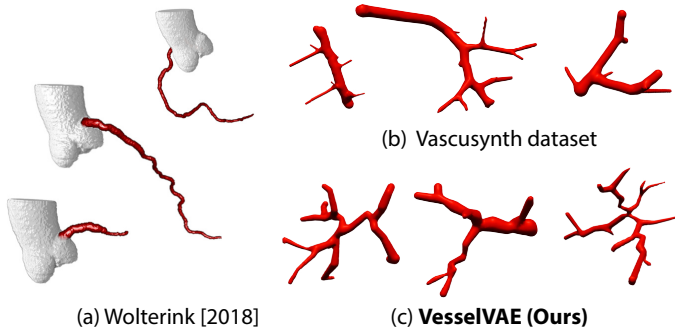


Fig. 6. (a) Vessel geometries generated by Wolterink et al. (2018). The evaluation is limited to a visual comparison due to the lack of access to the original code or data. (b) Vessel geometries generated using the method presented in Hamarneh and Jassi (2010). (c) Vessel geometries generated by our method when trained on (b). While occasionally struggling with unrealistic angles, VesselVAE effectively captures the underlying characteristics of the data, demonstrating a similar expressive power to the parametric method proposed by Hamarneh and Jassi (2010).

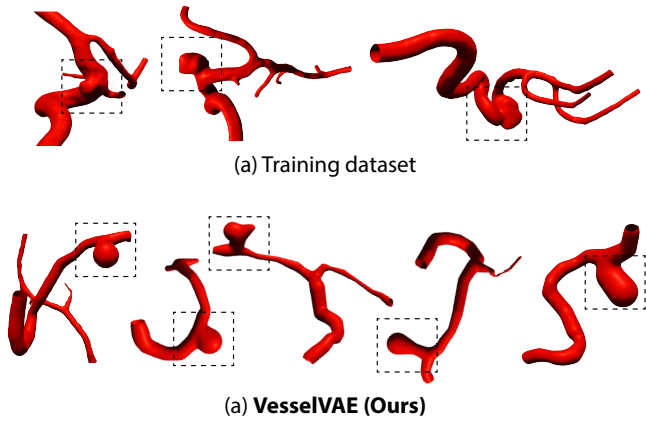


Fig. 7. (a) Vessels with aneurysms from the Aneurisk dataset. (b) Vessels with aneurysms generated by VesselVAE.

of the best-performing models for trees of maximum height 10.

To identify the best-performing scheme, we computed the average Earth Mover’s Distance (EMD) across all metrics—Radius, Tortuosity, and Length—for each row in Table 3. We then averaged the EMD for each weighting scheme, resulting in a single EMD value per scheme (Intra: *Uniform*=0.928, *Depth*=0.938, *Sub-tree*=0.933; Aneurisk: *Uniform*=0.87, *Depth*=0.87, *Sub-tree*=0.93). In the Aneurisk dataset, the sub-tree size weighting scheme exhibited superior performance, while in the Intra dataset, the depth-based weighting scheme achieved slightly better results compared to the others. This variation is likely attributable to the greater number of ramifications in the Aneurisk dataset (see Tab. 1 for dataset statistics), which has a stronger influence on the computation of loss weights. Conversely, the Intra dataset, with its fewer ramifications, showed comparable performance across both schemes. This highlights the role of this weight parameter in the autoencoder’s capability to accurately synthesize vasculature geometry.

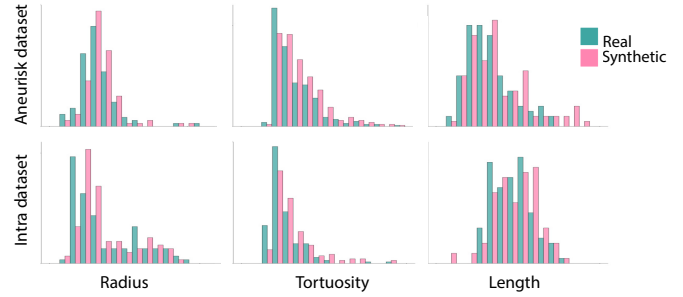


Fig. 8. Quantitative evaluation of generated vessel samples. The histograms display the distributions of each evaluated metric. Data generated by VesselVAE is labeled as *synthetic* (pink), while data from the datasets is labeled as *real* (blue). All histograms are computed from vessels with maximum height 10 and resampling ϵ 0.2

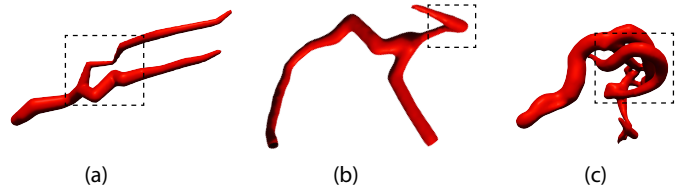


Fig. 9. Examples of VesselVAE generations exhibiting implausible angles (a, b) and self-intersections (c).

5. Discussion and Limitations

Our experiments utilized two open-source datasets of cerebral vasculature, resampled at different rates to show the impact on evaluation metrics. Results indicate that complexity increases with tree height, leading to good results with lower tree depths and suboptimal outcomes at the highest depths tested. While we experimentally found an optimal bottleneck size in our experiments, we hypothesize that the recursive encoding framework may lose information with high hierarchies. A per-branch evaluation could offer deeper insights (as proposed by Kuipers et al.). However, it requires labeled data which is not available in our setting. Additionally, the generated geometries might show self-intersections. This issue arises because, although the model effectively generates plausible geometries, it does not enforce strict constraints to eliminate self-intersections. In the future, we would like to incorporate restrictions into the generative model to avoid such artifacts. Furthermore, while our method synthesizes vessels highly similar to those in the training dataset, some exhibit implausible angles. This suggests the model struggles with angle learning. Potential improvements include adding an attribute for angles, exploring different angle representations, or resampling arteries with greater detail on curves. Examples of failed cases can be seen in Fig. 9.

6. Conclusions

We have presented a novel approach for synthesizing blood vessel models using a Recursive variational Neural Network. Our method enables efficient encoding and decoding of binary tree structures and produces high-quality synthesized models.

Our findings highlight the versatility of our network architecture, demonstrating its ability to synthesize blood vessels across different datasets, including those with aneurysms. Additionally, our approach outperforms recent state-of-the-art methods by more accurately replicating intricate vascular characteristics while producing more realistic and diverse geometries. In the future, we aim to explore other surface representations e.g. the zero level set in a differentiable neural implicit (INR) Sinha and Hamarneh (2024); Alblas *et al.* (2022). This could lead to more accurate and efficient modeling of blood vessels and potentially other non-tree-like structures such as capillary networks. Another potential direction is the development of an autoregressive model utilizing a tokenized representation of the tree, enabling coherent generation and supporting conditional outputs. Overall, our proposed approach shows potential for improving 3D blood vessel geometry synthesis and supporting the development of clinical tools that could benefit healthcare professionals.

Acknowledgments

This project was supported by grants from Salesforce, USA (Einstein AI 2020), National Scientific and Technical Research Council (CONICET), Argentina (PIP 2021-2023 GI - 11220200102981CO), and Universidad Torcuato Di Tella, Argentina.

Conflict of interest statement

The authors have no conflicts to disclose.

References

- Achlioptas, P., Diamanti, O., Mitliagkas, I., Guibas, L., 2018. Learning representations and generative models for 3d point clouds, in: International conference on machine learning, PMLR. pp. 40–49.
- Alblas, D., Brune, C., Wolterink, J.M., 2021. Deep learning-based carotid artery vessel wall segmentation in black-blood mri using anatomical priors. arXiv preprint arXiv:2112.01137 .
- Alblas, D., Brune, C., Yeung, K.K., Wolterink, J.M., 2022. Going off-grid: Continuous implicit neural representations for 3d vascular modeling, in: Statistical Atlases and Computational Models of the Heart. Regular and CM-RxMotion Challenge Papers: 13th International Workshop, STACOM 2022, Held in Conjunction with MICCAI 2022, Singapore, September 18, 2022, Revised Selected Papers, Springer Nature Switzerland. pp. 79–90.
- Aneurisk-Team, 2012. AneuriskWeb project website, <http://ecm2.mathcs.emory.edu/aneuriskweb>. Web Site. URL: <http://ecm2.mathcs.emory.edu/aneuriskweb>.
- Banerjee, T., Poddar, S., Bhattacharjee, S., Song, Y.A., Orozaliev, A., Bhattacharya, B.B., 2020. Sample preparation with free-flowing biochips using microfluidic binary-tree network, in: 2020 IEEE International Symposium on Circuits and Systems (ISCAS), IEEE. pp. 1–5.
- van Breugel, B., Liu, T., Oglic, D., van der Schaar, M., 2024. Synthetic data in biomedicine via generative artificial intelligence. *Nature Reviews Bioengineering* , 1–14.
- Bullitt, E., Gerig, G., Aylward, S., Joshi, S., Smith, K., Ewend, M., Lin, W., 2003a. Vascular attributes and malignant brain tumors, in: Medical Image Computing and Computer-Assisted Intervention-MICCAI 2003: 6th International Conference, Montréal, Canada, November 15-18, 2003. Proceedings 6, Springer. pp. 671–679.
- Bullitt, E., Gerig, G., Pizer, S.M., Lin, W., Aylward, S.R., 2003b. Measuring tortuosity of the intracerebral vasculature from mra images. *IEEE transactions on medical imaging* 22, 1163–1171.
- Cuntz, H., Forstner, F., Borst, A., Häusser, M., 2010. One rule to grow them all: a general theory of neuronal branching and its practical application. *PLoS computational biology* 6, e1000877.
- Deo, Y., Lin, F., Dou, H., Cheng, N., Ravikumar, N., Frangi, A., Lassila, T., 2024. Few-shot learning in diffusion models for generating cerebral aneurysm geometries, in: *Lecture Notes in Computer Science*, Springer Nature.
- Douglas, D.H., Peucker, T.K., 1973. Algorithms for the reduction of the number of points required to represent a digitized line or its caricature. *Cartographica: the international journal for geographic information and geovisualization* 10, 112–122.
- Feldman, P., Fainstein, M., Siless, V., Delrieux, C., Iarussi, E., 2023. Vesselvae: Recursive variational autoencoders for 3d blood vessel synthesis, in: International Conference on Medical Image Computing and Computer-Assisted Intervention, Springer. pp. 67–76.
- Galarreta-Valverde, M.A., Macedo, M.M., Mekkaoui, C., Jackowski, M.P., 2013. Three-dimensional synthetic blood vessel generation using stochastic l-systems, in: *Medical Imaging 2013: Image Processing*, SPIE. pp. 414–419.
- Goodfellow, I., Pouget-Abadie, J., Mirza, M., Xu, B., Warde-Farley, D., Ozair, S., Courville, A., Bengio, Y., 2020. Generative adversarial networks. *Communications of the ACM* 63, 139–144.
- Hamarneh, G., Jassi, P., 2010. Vascusynth: Simulating vascular trees for generating volumetric image data with ground-truth segmentation and tree analysis. *Computerized medical imaging and graphics* 34, 605–616.
- Higgins, I., Matthey, L., Pal, A., Burgess, C., Glorot, X., Botvinick, M., Mohamed, S., Lerchner, A., 2017. beta-vae: Learning basic visual concepts with a constrained variational framework, in: International conference on learning representations.
- Ho, J., Jain, A., Abbeel, P., 2020. Denoising diffusion probabilistic models. *Advances in Neural Information Processing Systems* 33, 6840–6851.
- Jumper, J., Evans, R., Pritzel, A., Green, T., Figurnov, M., Ronneberger, O., Tunyasuvunakool, K., Bates, R., Žídek, A., Potapenko, A., et al., 2021. Highly accurate protein structure prediction with alphafold. *nature* 596, 583–589.
- Kazemina, S., Baur, C., Kuijper, A., van Ginneken, B., Navab, N., Albarqouni, S., Mukhopadhyay, A., 2020. Gans for medical image analysis. *Artificial Intelligence in Medicine* 109, 101938.
- Kuipers, T.P., Konduri, P.R., Marquering, H., Bekkers, E.J., 2024. Generating cerebral vessel trees of acute ischemic stroke patients using conditional set-diffusion, in: *Medical Imaging with Deep Learning*.
- Lan, H., Updegrove, A., Wilson, N.M., Maher, G.D., Shadden, S.C., Marsden, A.L., 2018. A re-engineered software interface and workflow for the open-source simvascular cardiovascular modeling package. *Journal of biomechanical engineering* 140, 024501.
- Lang, S., Müller, B., Dominietto, M.D., Cattin, P.C., Zanette, I., Weitkamp, T., Hieber, S.E., 2012. Three-dimensional quantification of capillary networks in healthy and cancerous tissues of two mice. *Microvascular research* 84, 314–322.
- Lawaetz, J., Kristensen, J.S.S., Nayahangan, L.J., Van Herzeele, I., Konge, L., Eiberg, J.P., 2021. Simulation based training and assessment in open vascular surgery: a systematic review. *European Journal of Vascular and Endovascular Surgery* 61, 502–509.
- Le Bras, A., Boustia, F., Janot, K., Le Pabic, E., Ouvrard, M., Fougereou-Leurent, C., Ferre, J.C., Gauvrit, J.Y., Eugene, F., 2023. Rehearsals using patient-specific 3d-printed aneurysm models for simulation of endovascular embolization of complex intracranial aneurysms: 3d sim study. *Journal of Neuroradiology* 50, 86–92.
- Lee, J.J., Li, B., Benes, B., 2023. Latent l-systems: Transformer-based tree generator. *ACM Transactions on Graphics* 43, 1–16.
- Li, J., Xu, K., Chaudhuri, S., Yumer, E., Zhang, H., Guibas, L., 2017. Grass: Generative recursive autoencoders for shape structures. *ACM Transactions on Graphics (TOG)* 36, 1–14.
- Li, M., Patil, A.G., Xu, K., Chaudhuri, S., Khan, O., Shamir, A., Tu, C., Chen, B., Cohen-Or, D., Zhang, H., 2019. Grains: Generative recursive autoencoders for indoor scenes. *ACM Transactions on Graphics (TOG)* 38, 1–16.
- Looks, M., Herreshoff, M., Hutchins, D., Norvig, P., 2017. Deep learning with dynamic computation graphs. arXiv preprint arXiv:1702.02181 .
- Lorensen, W.E., Cline, H.E., 1998. Marching cubes: A high resolution 3d surface construction algorithm, in: *Seminal graphics: pioneering efforts that shaped the field*, pp. 347–353.
- Merrem, A., Bartzsch, S., Laissue, J., Oelfke, U., 2017. Computational mod-

- elling of the cerebral cortical microvasculature: effect of x-ray microbeams versus broad beam irradiation. *Physics in Medicine & Biology* 62, 3902.
- Mou, L., Lin, J., Zhao, Y., Liu, Y., Ma, S., Zhang, J., Lv, W., Zhou, T., Frangi, A.F., Zhao, Y., 2024. Costa: A multi-center multi-vendor tof-mra dataset and a novel cerebrovascular segmentation network. *IEEE Transactions on Medical Imaging*.
- Murthy, V.L., Naya, M., Foster, C.R., Hainer, J., Gaber, M., Dorbala, S., Charytan, D.M., Blankstein, R., Di Carli, M.F., 2012. Coronary vascular dysfunction and prognosis in patients with chronic kidney disease. *JACC: Cardiovascular Imaging* 5, 1025–1034.
- Nash, C., Ganin, Y., Eslami, S.A., Battaglia, P., 2020. Polygen: An autoregressive generative model of 3d meshes, in: *International conference on machine learning*, PMLR. pp. 7220–7229.
- Park, J.J., Florence, P., Straub, J., Newcombe, R., Lovegrove, S., 2019. DeepSDF: Learning continuous signed distance functions for shape representation, in: *Proceedings of the IEEE/CVF conference on computer vision and pattern recognition*, pp. 165–174.
- Patil, A.G., Ben-Eliezer, O., Perel, O., Averbuch-Elor, H., 2020. Read: Recursive autoencoders for document layout generation, in: *Proceedings of the IEEE/CVF Conference on Computer Vision and Pattern Recognition Workshops*, pp. 544–545.
- Prabhakar, C., Shit, S., Musio, F., Yang, K., Amiranashvili, T., Paetzold, J.C., Li, H.B., Menze, B., 2024. 3d vessel graph generation using denoising diffusion. *arXiv preprint arXiv:2407.05842*.
- Ramer, U., 1972. An iterative procedure for the polygonal approximation of plane curves. *Computer graphics and image processing* 1, 244–256.
- Ramesh, A., Pavlov, M., Goh, G., Gray, S., Voss, C., Radford, A., Chen, M., Sutskever, I., 2021. Zero-shot text-to-image generation, in: *International conference on machine learning*, Pmlr. pp. 8821–8831.
- Rauch, N., Harders, M., 2021. Interactive Synthesis of 3D Geometries of Blood Vessels, in: Theisel, H., Wimmer, M. (Eds.), *Eurographics 2021 - Short Papers*, The Eurographics Association.
- Roman, M.J., Kizer, J.R., Best, L.G., Lee, E.T., Howard, B.V., Shara, N.M., Devereux, R.B., 2012. Vascular biomarkers in the prediction of clinical cardiovascular disease: the strong heart study. *Hypertension* 59, 29–35.
- Schneider, M., Reichold, J., Weber, B., Székely, G., Hirsch, S., 2012. Tissue metabolism driven arterial tree generation. *Medical image analysis* 16, 1397–1414.
- Siddiqui, Y., Alliegro, A., Artemov, A., Tommasi, T., Sirigatti, D., Rosov, V., Dai, A., Nießner, M., 2024. Meshgpt: Generating triangle meshes with decoder-only transformers, in: *Proceedings of the IEEE/CVF Conference on Computer Vision and Pattern Recognition*, pp. 19615–19625.
- Sinha, A., Hamarneh, G., 2024. Representing anatomical trees by denoising diffusion of implicit neural fields. *arXiv preprint arXiv:2403.08974*.
- Socher, R., 2014. *Recursive deep learning for natural language processing and computer vision*. Stanford University.
- Socher, R., Lin, C.C., Manning, C., Ng, A.Y., 2011. Parsing natural scenes and natural language with recursive neural networks, in: *Proceedings of the 28th international conference on machine learning (ICML-11)*, pp. 129–136.
- Talou, G.D.M., Safaei, S., Hunter, P.J., Blanco, P.J., 2021. Adaptive constrained constructive optimisation for complex vascularisation processes. *Scientific Reports* 11, 1–22.
- Taylor, C.A., Petersen, K., Xiao, N., Sinclair, M., Bai, Y., Lynch, S.R., Upde-Pac, A., Schaap, M., 2023. Patient-specific modeling of blood flow in the coronary arteries. *Computer Methods in Applied Mechanics and Engineering* 417, 116414.
- Tetteh, G., Efremov, V., Forkert, N.D., Schneider, M., Kirschke, J., Weber, B., Zimmer, C., Piraud, M., Menze, B.H., 2020. Deepvesselnet: Vessel segmentation, centerline prediction, and bifurcation detection in 3-d angiographic volumes. *Frontiers in Neuroscience*, 1285.
- Vaswani, A., Shazeer, N., Parmar, N., Uszkoreit, J., Jones, L., Gomez, A.N., Kaiser, Ł., Polosukhin, I., 2017. Attention is all you need. *Advances in neural information processing systems* 30.
- Wolterink, J.M., Leiner, T., Isgum, I., 2018. Blood vessel geometry synthesis using generative adversarial networks. *arXiv preprint arXiv:1804.04381*.
- Wu, J., Hu, Q., Ma, X., 2013. Comparative study of surface modeling methods for vascular structures. *Computerized Medical Imaging and Graphics* 37, 4–14.
- Wu, J., Zhang, C., Xue, T., Freeman, B., Tenenbaum, J., 2016. Learning a probabilistic latent space of object shapes via 3d generative-adversarial modeling. *Advances in neural information processing systems* 29.
- Xu, M., Niyato, D., Chen, J., Zhang, H., Kang, J., Xiong, Z., Mao, S., Han, Z., 2023. Generative ai-empowered simulation for autonomous driving in vehicular mixed reality metaverses. *arXiv preprint arXiv:2302.08418*.
- Yan, W., Zhang, Y., Abbeel, P., Srinivas, A., 2021. Videogpt: Video generation using vq-vae and transformers. *arXiv preprint arXiv:2104.10157*.
- Yang, G., Huang, X., Hao, Z., Liu, M.Y., Belongie, S., Hariharan, B., 2019. Pointflow: 3d point cloud generation with continuous normalizing flows, in: *Proceedings of the IEEE/CVF international conference on computer vision*, pp. 4541–4550.
- Yang, X., Xia, D., Kin, T., Igarashi, T., 2020. Intra: 3d intracranial aneurysm dataset for deep learning, in: *Proceedings of the IEEE/CVF Conference on Computer Vision and Pattern Recognition*, pp. 2656–2666.
- Zamir, M., 2001. Arterial branching within the confines of fractal l-system formalism. *The Journal of general physiology* 118, 267–276.

Supplementary Material

Layer name	Input shape	Output shape	Layer name	Input shape	Output shape
Encoder			Decoder		
fc1	4	512	fc1	64	256
fc2	512	64	fc_left1	256	256
right_fc1	64	512	fc_left2	256	64
right_fc2	512	64	fc_right1	256	256
left_fc1	64	512	fc_right2	256	64
left_fc2	512	64	fc2	256	64
fc3	128	64	fc3	64	4
Supplementary Networks					
$f_\mu + f_\sigma$			g_z		
fc1	128	512	fc1	64	256
fc2mu	512	128	fc2	256	256
fc2var	512	128	fc3	256	64
			Classifier		
-	-	-	fc1	64	256
-	-	-	fc2	256	256
-	-	-	fc3	256	3

Table 1s. Our proposed method consists of two primary components: a recursive Encoder and a recursive Decoder. All layers in each component are fully connected with leaky rectified linear unit (Leaky ReLU) activations, except for g_z which uses the Tanh. The Classifier is a sub-network inside the Decoder that predicts a label for each node in the input graph.

	Encoder	Decoder	$f_\mu + f_\sigma$	g_z	Classifier
Trainable parameters	527616	197828	98944	9880	83203

Table 2s. Summary of trainable parameters for each component.

		Vascusynth													
		Cosine similarity \uparrow							Earth Mover Distance \downarrow						
Weighting Scheme	Max. Height	ϵ	Radius			Tortuosity		Length		Radius		Tortuosity		Length	
			M	CI		M	CI	M	CI	M	CI	M	CI	M	CI
Depth	5	0.2	.96	(.95 .97)		.51	(.47 .56)	.80	(.74 .85)	.42	(.32 .53)	2.67	(1.83 3.52)	.44	.3 .59
Sub-tree			.92	(.89 .95)		.78	(.74 .83)	.93	(.91 .95)	.54	(.45 .64)	3.35	(2.68 4.01)	.46	(.33 .58)
Depth		0.1	.92	(.89 .94)		.87	(.83 .91)	.74	(.64 .83)	.41	(.3 .52)	3.64	(2.85 4.43)	1.05	(.91 1.19)
Sub-tree			.9	(.88 .92)		.6	(.55 .64)	.85	(.82 .87)	.69	(.52 .85)	5.4	(4.33 6.47)	1.77	(1.59 1.94)
Depth	10	0.2	.87	(.85 .89)		.93	(.91 .96)	.88	(.85 .9)	.61	(.42 .8)	1.95	(1.43 2.47)	.46	(.37 .55)
Sub-tree			.91	(.88 .92)		.85	(.83 .86)	.96	(.95 .97)	.97	(.7 1.23)	1.18	(.93 1.44)	.85	(.71 .98)
Depth		0.1	.96	(.95 .97)		.91	(.89 .93)	.83	(.81 .85)	.5	(.38 .62)	2.68	(1.86 3.49)	.66	(.54 .79)
Sub-tree			.89	(.88 .9)		.63	(.55 .71)	.82	(.79 .84)	1.0	(0.9 1.11)	3.33	(1.91 4.76)	1.57	(1.42 1.72)
Depth	15	0.2	.5	(.47 .53)		.65	(.59 .72)	.56	(.49 .63)	2.65	(2.34 2.96)	1.38	(1.02 1.74)	2.9	(2.53 3.26)
Sub-tree			.82	(.79 .85)		.76	(.68 .84)	.87	(.85 .89)	1.4	(1.28 1.53)	2.41	(1.51 3.3)	.77	(.64 .89)
Depth		0.1	.86	(.82 .9)		.82	(.79 .85)	.74	(.68 .79)	.87	(.79 .94)	1.41	(1.02 1.79)	3.69	(3.07 4.32)
Sub-tree			.75	(.71 .78)		.43	(.26 .6)	.43	(.38 .47)	1.98	(1.82 2.14)	2.81	(1.68 3.94)	2.97	(2.8 3.13)

Table 3s. Cosine Similarity and Earth Mover Distance for all the evaluated metrics with resampling parameter $\epsilon = 0.1$ and $\epsilon = 0.2$, with trees trimmed to depths 5, 10 and 15. We run the experiments 10 times with random initial vectors and reported the mean values (M) and 95 % confidence intervals (CI) for VesselVAE trained on synthetic data generated with Hamarneh and Jassi (2010). We attribute the larger performance drop on Vascusynth, especially at greater depths to a mismatch between VesselVAE’s inductive biases and the synthetic nature of the data. The VesselVAE architecture was designed and tuned for anatomical realism based on real datasets (Aneurisk and Intra), whereas Vascusynth is generated via a parametric algorithm. We hypothesize, the model is being pushed to generalize beyond the structural patterns it was intended to capture.

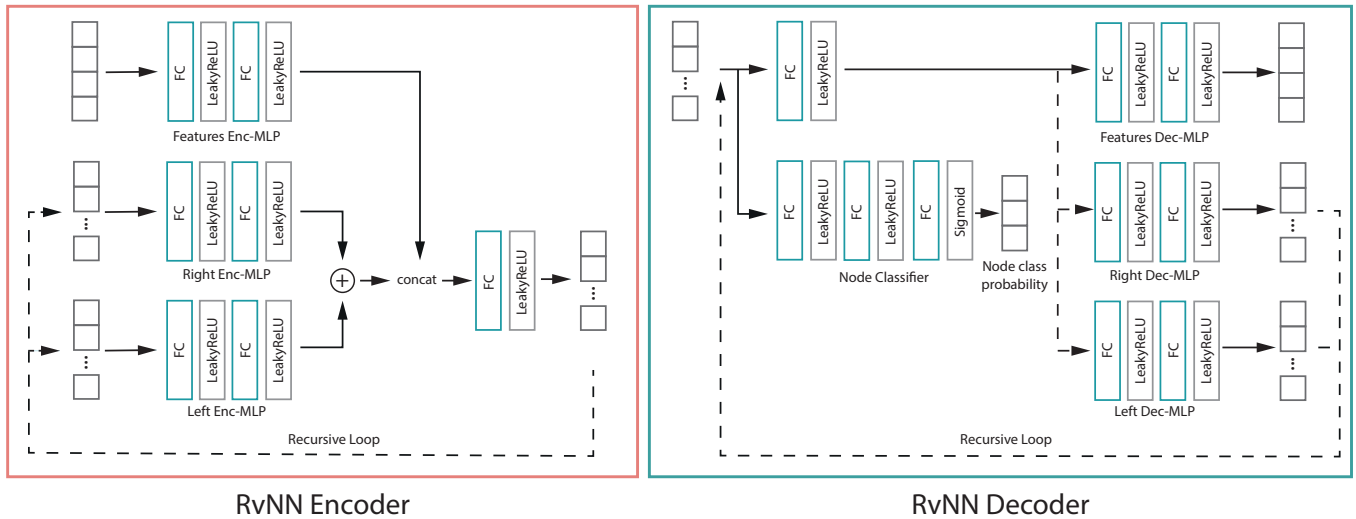


Fig. 1s. Layers of the Encoder and Decoder networks comprising branches of fully-connected layers followed by leaky ReLU activations. Notice that right/left Enc-MLPs of the Encoder only execute when the incoming tree requires it. Similarly, the Decoder only uses right/left Dec-MLPs when the Node Classifier predicts bifurcations.